Science

AAAS

Supplementary Materials for

Field-induced transition from even to odd parity superconductivity in CeRh$_2$As$_2$

S. Khim,[1†*] J. F. Landaeta,[1†] J. Banda,[1] N. Bannor,[1] M. Brando,[1] P. M. R. Brydon,[2]
D. Hafner,[1] R. Küchler,[1] R. Cardoso–Gil,[1] U. Stockert,[1] A. P. Mackenzie,[1,3]
D. F. Agterberg,[4] C. Geibel,[1] and E. Hassinger[1,5*]
[1]Max Planck Institute for Chemical Physics of Solids, 01187 Dresden, Germany
[2]Department of Physics and MacDiarmid Institute for Advanced Materials and Nanotechnology,
University of Otago, P.O. Box 56, Dunedin 9054, New Zealand
[3]Scottish Universities Physics Alliance, School of Physics and Astronomy,
University of St Andrews, St Andrews KY16 9SS, United Kingdom
[4]Department of Physics, University of Wisconsin–Milwaukee,
Milwaukee, Wisconsin 53201, USA
[5]Technical University Munich, Physics department, 85748 Garching, Germany

[†]These authors contributed equally to the research.
[*]Correspondence to: elena.hassinger@cpfs.mpg.de and seunghyun.khim@cpfs.mpg.de

This PDF file includes:

Materials and Methods
Supplementary Text
Figs. S1 to S8
Tables S1 and S2
Eqs. S1 to S17

Materials and Methods

Single crystal synthesis

Single crystals of $CeRh_2As_2$ and $LaRh_2As_2$ were grown in Bi flux. Elemental metals with the ratio of Ce(La):Rh:As:Bi = 1:2:2:30 were placed in an alumina crucible which was subsequently sealed in a quartz tube filled with argon at a partial pressure of 300 mbar. The ampule was heated to 1150 ºC for 4 days and slowly cooled down to 700 ºC for a week. Grown single crystals were extracted by selectively removing the Bi flux in diluted nitric acid. The composition and the crystal structure were determined by Energy-dispersive x-ray spectroscopy (EDXS) and both powder and single crystal x-ray diffraction analysis. Detailed crystal structure information is shown in Fig. S1, Table S1 and S2.

Specific heat

The specific heat measurements were carried out using the relaxation time method in a Quantum Design Physical Property Measurements System (PPMS) down to temperatures of 0.5 K, and a custom compensated heat-pulse calorimeter for temperatures between 0.04 and 100 K in magnetic fields up to 12 T (*46*). The specific-heat data of $LaRh_2As_2$ were used to subtract a non-electronic contribution.

Thermopower

The thermopower was measured within the *ab*-plane between 2.5 K and 290 K using a modified sample holder for the thermal transport option of a PPMS. The instrument applies a relaxation time method. A low-frequency square-wave heat pulse is generated by a resistive heater. The temperature difference along the sample is measured with two calibrated bare-chip Cernox sensors.

Ac susceptibility

The magnetic ac-susceptibility was measured using a homemade set of compensated pick-up coils of 2 mm length and 6000 turns each. The inner and outer diameter was 1.8 mm and 5 mm, respectively. A superconducting modulation coil produced the excitation field of 175 μT at 5 Hz. The output signal of the pick-up coils was amplified using a low temperature transformer (LTT-m from CMR) with a winding ratio 1:100 and a low noise amplifier SR560 from Stanford Research Systems. Our setup uses a National Instruments 24 bits PXIe-4463 signal generator and 24 bits PXIe-4492 oscilloscope as data acquisition system with digital lock-in amplification. The ac-susceptibility measurements were performed for $H \parallel ab$ and $H \parallel c$ using a small single crystal of a volume of $\sim$500 μm^3 down to 45 mK in an external magnetic field of up to 15 T in a MX400 Oxford dilution refrigerator. The data from temperature sweeps were normalized to their respective value in the normal state at 0.5 K for all the magnetic fields applied. For the field sweeps, the absolute value of the signal at different temperatures is given, normalized to the field-dependent value in the normal state at 0.35 K. Low field data were removed because of noise due to flux jumps in a superconducting magnet. The complete data is shown in Fig. S5 and S7.

Resistivity

For resistivity measurements a standard four-point method was employed with current and voltage contacts along a line perpendicular to the *c*-axis using an excitation current of 100 μA. The four contacts were spot-welded on the sample using gold wires with 25 μm diameter.

The signal was amplified by a low-temperature transformer with a winding ratio of 1:100 and the output of the transformer was measured using a SR830 lock-in amplifier at a frequency of 113.7 Hz.

Magnetostriction

The linear magnetostriction coefficient $\lambda = (1/L)(dL/dH)_T$ was measured using a miniaturized high-resolution capacitance dilatometer of CuBe (*47*). The length change ΔL of the sample was measured perpendicular to the c-axis. Using an ultrahigh-resolution Andeen-Hagerling capacitance bridge, the absolute value of the dilatometer capacitance was measured with a resolution of 10^{-6} pF, corresponding to a length resolution of 0.02 Å. The experiments were carried out in an Oxford Instruments K100 dilution refrigerator with a superconducting magnet in magnetic fields up to 5 T.

Magnetization

Magnetization measurements were carried out using a commercial vibrating sample magnetometer, Quantum Design Magnetic Property Measurement System (MPMS-VSM), for the high-temperature range between 1.8 and 380 K, and a custom high-resolution capacitive Faraday magnetometer for the low-temperature range between 0.05 and 2 K and magnetic fields up to 12 T (*48*).

Supplementary Text

Note on the thermopower of Kondo-lattice systems

The T-dependence of the thermopower was measured down to 2.5 K. The saturation of S/T to a constant value in the zero-temperature limit is usually seen at lower T. The thermopower of CeRh$_2$As$_2$ changes sign to negative S below about 4 K. Since $S \rightarrow 0$ in the zero T limit, $S(T)$ has to go through a minimum at lower T. A phonon drag effect is expected to be negligible due to the crystal quality with low RRR values. The thermal conductivity measured simultaneously with the thermopower increases monotonously with increasing T. It shows no peak at low T due to Umklapp scattering as typically seen in very clean single crystals. A phonon-drag peak in $S(T)$ is usually accompanied by such a peak in thermal conductivity. Rather, the features in $S(T)$ are caused by a combination of Kondo scattering and thermal population of higher CEF levels: In the data we observe a maximum at about 80 K and a shoulder at about 15 K. In Kondo lattice systems the main contribution to the thermopower is given by the Kondo scattering on the ground-state doublet of the crystalline electric field (CEF) and on the thermally populated higher multiplet states. From the CEF analysis (3 doublets) we found that the first excited level is located at about 30 K (similar value as the Kondo temperature) and the second level at about 180 K. From the position of the maximum in $S(T)$ theoretical calculations predict $T_{max} = (0.3 - 0.6)$ ΔCEF/k_B giving ΔCEF/$k_B \sim 130 - 270$ K in agreement with the ΔCEF/$k_B \sim 180$ K from the CEF analysis. A comprehensive study can be found in this work (*49*).

Subtraction of the nuclear Schottky contribution in the specific heat data at low temperatures

The low-T heat capacity of CeRh$_2$As$_2$ was measured in zero magnetic field and in an external field aligned along both the c-axis ($H \parallel c$) and the basal ab-plane ($H \parallel ab$) of the tetragonal crystalline structure. In all measurements we observed upturns in C/T below $T \approx 0.2$

K, the intensity of which increases systematically with the square of the magnetic field. An example is shown in Fig. S2 in which the raw data for C/T are plotted versus T at zero field and at 10 T. At $\mu_0 H = 0$ the upturn is very weak and visible only below 0.06 K, but at $\mu_0 H \parallel ab = 10$ T (empty red circles) this effect is strong and visible below 0.2 K. With $\mu_0 H \parallel c = 10$ T (filled red circles), however, this contribution is not so distinct because it adds to that of the superconducting transition located at about 0.2 K.

These features are due to the nuclear contribution to the specific heat. Since the Ce atom has zero nuclear moment and the contribution from the Rh nuclear moment is relevant only well below 1 mK (50,51), the only relevant contribution to the specific heat originates from the ^{75}As atoms (100% abundance). ^{75}As atoms have nuclear angular momentum $I = 3/2$, a magnetic moment $\mu_I = g_N\mu_N I$ with $\mu_N = 5.05 \times 10^{-27}$ J/T (nuclear magneton) and g_N, the nuclear g-factor, and an electric quadrupole moment $Q = 0.3 \times 10^{-28}$ m^2. In the tetragonal unit cell of CeRh$_2$As$_2$ they occupy two positions, As(1) and As(2) at which the field gradient eq is slightly different.

In zero magnetic field the splitting of the nuclear energy levels is given by $\Delta\varepsilon = (1/2)e^2qQ$ which corresponds to a (NQR) frequency $\nu_Q = \Delta/h$. In magnetic field, however, or in magnetically ordered compounds the energy level degeneracy is further lifted and the splitting is proportional to the effective magnetic field at the nuclei $\Delta\varepsilon = - g_N\mu_N B_{\mathrm{eff}}$ (Zeeman energy). This energy splitting $\Delta\varepsilon$ is mostly of the order of a few mK and therefore visible in specific heat data as the high-temperature part of a Schottky anomaly which is proportional to T^{-2} (see, e.g., refs. 51,52) and is proportional to B^2.

The specific heat at low temperatures is then given by three contributions:

$$ C = C_n + C_{el} + C_{ph} = \frac{\alpha}{T^2} + \gamma T + \beta T^3 $$

, where $C_{\mathrm{el}} + C_{\mathrm{ph}}$ are the electronic and phonon contributions and α is the proportional factor in the nuclear Schottky specific heat. The phonon contribution is very small below 1 K and can safely be ignored in this analysis. Since the C_n contribution is strong at low temperatures, to extract the α parameter it is convenient to plot the data as:

$$ \frac{C(T)}{T} = \frac{\alpha}{T^3} + \gamma $$

and extrapolate the linear-in-T behavior at very low T, i.e., in the range where the nuclear term dominates. This is exemplarily shown in the inset of Fig. S2 in which C/T vs T^{-3} is plotted for the data at 10 T in both field directions. The data can reliably be fitted with a linear function in the low-T range. The fits yield: $\alpha_{ab}(10\ \mathrm{T}) = 3.36 \times 10^{-4}$ JK/mol and $\alpha_c(10\ \mathrm{T}) = 3.49 \times 10^{-4}$ JK/mol. Both data sets show a similar α which is expected since the effective field at the As nuclei is very close to the external applied field. After having extracted α at all fields we have plotted α versus B^2 to check consistency with the Schottky equation. A linear fit to the data yields a zero field nuclear parameter: $\alpha(0\ \mathrm{T}) = (1.57 \pm 0.2) \times 10^{-5}$ JK/mol. We have subtracted the nuclear contribution from all data presented and analyzed in the main text. A more detailed analysis will be presented in a forthcoming paper.

Crystal electric field analysis

The crystal field Hamiltonian for Ce in the tetragonal environment is given by $H = B_2^0 O_2^0 + B_4^0 O_4^0 + B_4^4 O_4^4$ where B_n^m are the crystal electric field parameters and O_n^m are Stevens operators (53,54). The magnetic susceptibility is calculated as

$$\chi_{CEF,i} = N_A(g_J\mu_B)^2 \frac{1}{Z}\left(\sum_{m\neq n} 2|\langle m|J_i|n\rangle|^2 \frac{1 - e^{-(\beta(E_n - E_m))}}{E_n - E_m}e^{-\beta E_n} + \sum_n |\langle n|J_i|n\rangle|^2\beta e^{-\beta E_n}\right)$$

, where $Z = \sum_n e^{-\beta E_n}$, $\beta = 1/k_B T$, and $i = x, y, z$. The calculated inverse magnetic susceptibility including the molecular field contribution λ_i as $\chi_i^{-1} = \chi_{CEF,i}^{-1} - \lambda_i$ is given to fit the experimental data. The presented fits (see Fig. S3) are obtained from the doublet ground state $|\Gamma_7^{(1)}\rangle = 0.88\ |\mp 3/2\rangle - 0.47\ |\pm 5/2\rangle$ with the first excited state $|\Gamma_6\rangle = |\pm 1/2\rangle$ at 30 K and the second excited level $|\Gamma_7^{(2)}\rangle = 0.47\ |\pm 3/2\rangle + 0.88\ |\mp 5/2\rangle$ at 180 K. λ_i is set to 36 mol/emu for both fields. These states are obtained from a diagonalization of the crystal field Hamiltonian with the parameters of $B_2^0 = 6.5$ K, $B_4^0 = 0.1$ K, and $B_4^4 = 2.8$ K. The energy splitting for the two lower-lying states is comparable to the Kondo energy scale of $T_K \sim 20$ - 40 K, which is given by the relation of $S_{mag}(T_K/2) = (1/2)R\ln x$, where $x = 2$ for a doublet and 4 for a quartet ground state. The ground state can have a nature of a quartet state when the wave function of the first-excited level partially contributes to the ground state through a possible mixing channel such as Kondo interactions.

Role of magnetic field on superconductivity
To understand the key physics underlying the response of superconductivity to magnetic fields, it helps to rewrite the general Hamiltonian H_N as:

$$H_N = \epsilon_{00,k}\tau_0\sigma_0 + \epsilon_{x0,k}\tau_x\sigma_0 + \epsilon_{y0,k}\tau_y\sigma_0 + \epsilon_{zx,k}\tau_z\sigma_x + \epsilon_{zy,k}\tau_z\sigma_y + \epsilon_{zz,k}\tau_z\sigma_z. \quad (S1)$$

We have argued that $\epsilon_{zz,k}$ can be ignored since it corresponds to a long-range real-space hopping, so in the following we consider the limit $\epsilon_{zz,k} = 0$. The Hamiltonian H_N yields two bands with energies

$$E_{\pm,k} = \epsilon_{00,k} \pm \tilde{\epsilon}_k = \epsilon_{00,k} \pm \sqrt{\epsilon_{x0,k}^2 + \epsilon_{y0,k}^2 + \epsilon_{zx,k}^2 + \epsilon_{zy,k}^2}. \quad (S2)$$

Here we will consider the limit that $\tilde{\epsilon} \gg \Delta$ and $\tilde{\epsilon} \gg g\mu_B|H|$, that is the band separation is larger than the superconducting gap and the Zeeman energy.
We take the Zeeman Hamiltonian to be

$$H_Z = g_{ab}\mu_B(H_x\sigma_x + H_y\sigma_y)\tau_0 + g_z\mu_B H_z\sigma_z\tau_0. \quad (S3)$$

In the limit that the band splitting $\tilde{\epsilon} \gg g\mu B|H|$, we can express H_Z in the pseudospin basis, which is the eigenbasis of H_N. To define pseudospin, we note that the product of time-reversal (T) and inversion (I) symmetries imply that there are at least two degenerate states at each momentum. In particular, we can choose one of these states to be pseudospin-up and the degenerate pseudospin-down state is found by applying the symmetry TI to the pseudospin-up state. Note that since the pseudospin-up and down states are degenerate, we can choose any

linear combination of these to be our basis states. Here, we choose a pseudospin basis that shares the same rotation properties as usual spin under the point group operators of D_{4h} (55,56). Here we express the Pauli matrices for pseudospin as s_i.

When the Zeeman Hamiltonian is expressed in the pseudospin basis, there will be intraband and interband terms. The interband terms will not be changed appreciably by superconductivity because $\tilde{\epsilon} \gg \Delta$. However, the intraband terms will represent an effective pseudospin Zeeman field, which will then play a role similar to the usual Zeeman field in superconductivity without spin-orbit coupling. For either band, this intraband relationship between spin and pseudospin takes the form

$$
\begin{aligned}
\sigma_x &\to \gamma_{x,k} s_x + \gamma_{m,k} s_y \\
\sigma_y &\to \gamma_{m,k} s_x + \gamma_{y,k} s_y \\
\sigma_z &\to \gamma_{z,k} s_z.
\end{aligned}
\tag{S4}
$$

This shows that that field direction experienced by pseudospin is not generally the same as the applied field direction of the Zeeman field (here, these field directions are only the same for applied fields oriented along the z-axis). The form of these $\gamma_{i,k}$ is not particularly informative. However, it is possible to find the following useful relationship

$$
\begin{aligned}
\gamma_{x,k}^2 + \gamma_{m,k}^2 &= \frac{\epsilon_{x0,k}^2 + \epsilon_{y0,k}^2 + \epsilon_{xz,k}^2}{\epsilon_{x0,k}^2 + \epsilon_{y0,k}^2 + \epsilon_{xz,k}^2 + \epsilon_{yz,k}^2} \\
\gamma_{y,k}^2 + \gamma_{m,k}^2 &= \frac{\epsilon_{x0,k}^2 + \epsilon_{y0,k}^2 + \epsilon_{xy,k}^2}{\epsilon_{x0,k}^2 + \epsilon_{y0,k}^2 + \epsilon_{xz,k}^2 + \epsilon_{yz,k}^2} \\
\gamma_{z,k}^2 &= \frac{\epsilon_{x0,k}^2 + \epsilon_{y0,k}^2}{\epsilon_{x0,k}^2 + \epsilon_{y0,k}^2 + \epsilon_{xz,k}^2 + \epsilon_{yz,k}^2}.
\end{aligned}
\tag{S5}
$$

Pseudospin-singlet states

One consequence of Eq. S5 is that the magnitude of the pseudospin Zeeman field is in general smaller than that of the original Zeeman field. This has an immediate physical significance for the Pauli limiting field for an even parity, pseudospin-singlet superconductor that is independent of the pairing symmetry. For example, for an applied Zeeman field H_z, the effective magnitude of Zeeman field felt by the pseudospin is $\sqrt{\gamma_{z,k}} H_z < H_z$, so the Pauli field will be generally increased. Indeed, for a pseudospin-singlet state, only the magnitude of the pseudospin Zeeman field is needed to compute the Pauli limiting field (2). In general, this magnitude depends upon k, so that the Pauli limiting field will be expressed as an average over the Fermi surface. Since the $\gamma_{i,k}$ are non-zero, there will in general be Pauli limiting (albeit less than that for a usual spin-singlet superconductor). Notice that if $g_{ab} = g_z$ then Eq. S5 generally indicates that the Pauli limiting field is largest for the applied field along the z-direction since $\gamma_{z,k}^2 < \gamma_{x,k}^2 + \gamma_{m,k}^2, \gamma_{y,k}^2 + \gamma_{m,k}^2$, independent of the pairing symmetry of the pseudospin-singlet gap function.

Pseudospin-triplet states

For odd-parity, pseudospin-triplet states the Pauli limiting fields depend upon both the direction and magnitudes of the pseudospin Zeeman fields (2). It is therefore important to also

express the superconducting gap functions in the pseudospin basis. Here we consider explicitly states $\widetilde{\Delta}_e = \tau_0 \psi(k)$ and $\widetilde{\Delta}_o = \tau_z \psi(k)$ where $\psi(k)$ can be an even-parity pairing state describing the superconducting state in a Ce plane (and $\psi(k)$ can be of arbitrary symmetry, for example s-wave or d-wave). When the Ce planes are uncoupled, the $\widetilde{\Delta}_e$ and the $\widetilde{\Delta}_o$ states will be degenerate. Writing these two gap functions in the pseudospin basis yields

$$\widetilde{\Delta}_e = \tau_0 \psi(k) \rightarrow \psi(k) \tag{S6}$$

$$\widetilde{\Delta}_o = \tau_z \psi(k) \rightarrow \frac{\epsilon_{zx,k} s_x + \epsilon_{zy,k} s_y}{\sqrt{\epsilon_{x0,k}^2 + \epsilon_{y0,k}^2 + \epsilon_{xz,k}^2 + \epsilon_{yz,k}^2}} \psi(k). \tag{S7}$$

This shows explicitly that the odd-parity state becomes a pseudospin-triplet state. Importantly, this triplet state has no s_z component - the corresponding pseudospin-triplet d-vector is purely in-plane. Consequently, if the applied field in the pseudospin basis is purely along the z-direction, then the spin-susceptibility will be unchanged (since then $d \cdot \widetilde{H} = 0$ where $\widetilde{H}$ is the field in the pseudospin basis). Consequently, a c-axis Zeeman-field will not suppress the superconducting state at all, so the Pauli limiting field is formally "infinite" for all temperatures (note this conclusion is true provided we remain in the limit $\tilde{\epsilon} \gg g\mu_B|H|$.)

These general results then reveal the essential physics: for a field along the c-axis, a pseudospin-singlet state will have an enhanced, but not infinite Pauli field; while a pseudospin-triplet state (of the kind discussed here) will have an "infinite Pauli" field. This result is independent of the form of $\psi(k)$, which describes the pairing in a single Ce plane. This is the origin of the field induced transition. We also note these results can be generalized to include an odd parity spin-triplet state in a single Ce plane, provided it has a σ_z spin-triplet component and provided the spin-singlet component is the dominant component (if such a spin-triplet component is dominant, then it will be stable in zero-field, so no phase transition is expected for a field oriented along the c-axis). In general an admixture between spin-singlet and spin-triplet is allowed in a Ce plane, since these planes do not have inversion symmetry (*29,30*).

Semi-quantitative model

Since the general arguments above imply that a c-axis field driven transition between $\widetilde{\Delta}_e$ and $\widetilde{\Delta}_o$ is generic, it is useful to find a limit where the momentum dependence can be easily handled and the theory defined by simple constants to gain a semi-quantitative understanding. This can be done near the Γ-point together with the condition $t = t_{c,1} = t_{c,2}$. In this case,

$$\epsilon_{00,k} = m(k_x^2 + k_y^2) - \mu$$
$$\epsilon_{x0}, k = t \cos\left(\frac{k_z}{2}\right)$$
$$\epsilon_{y0}, k = t \sin\left(\frac{k_z}{2}\right)$$
$$\epsilon_{zx,k} = -\alpha k_y \tag{S8}$$
$$\epsilon_{zx,k} = \alpha k_x$$
$$\epsilon_{zz,k} = \lambda \sin k_z \, k_x k_y (k_x^2 - k_y^2) \approx 0$$

$$\tilde{\epsilon} = \sqrt{\alpha^2\left(k_x^2 + k_y^2\right) + t^2} = \sqrt{\alpha^2 k_F^2 + t^2}$$

, where the last line applies since we will be considering physics near the Fermi surface. It is also useful to consider simple s-wave superconductivity within a Ce layer, that is $\psi(k) = \Delta$. From the expression of the gap functions in the pseudospin basis and the form of the free energy, it is possible to find the ratio of the effective pairing interactions for the even (V_e) and odd-parity states (V_o),

$$\frac{V_o}{V_e} = \frac{\alpha^2 k_F^2}{\alpha^2 k_F^2 + t^2} = \frac{\tilde{\alpha}^2}{\tilde{\alpha}^2 + 1}. \tag{S9}$$

This reveals that both the even and odd-parity interactions are attractive, but the even-parity transition will have a higher transition temperature in zero field.

Even-parity state with in-plane field

Let us first consider only the Pauli field for this field orientation. For the pseudospin-singlet case, the Pauli fields are enhanced by the inverse square root of the factors given in Eq. S5 above. For our simple model, and using ϕ to give the polar angle on the cylindrical Fermi surface, for an applied field H_x applied along x yields the pseudospin magnetic field magnitude:

$$\tilde{H}_x(\phi) = H_x\sqrt{\gamma_{x,k}^2 + \gamma_{m,k}^2} = \frac{H_x\sqrt{1 + \tilde{\alpha}^2 \sin^2\phi}}{\sqrt{1 + \tilde{\alpha}^2}}. \tag{S10}$$

This expression reveals that the Pauli limiting field will be increased once $\tilde{\alpha} \neq 0$. This also yields the following expression for the upper critical field as a function of temperature

$$\log t = \Re \sum_{n=0}^{\infty} \left\langle \frac{1}{n + 1/2 + ig_{ab}\mu_B\tilde{H}_x(\phi)/(2\pi T_c t)} - \frac{1}{n + 1/2} \right\rangle_\phi \tag{S11}$$

, where the $\langle f \rangle_\phi$ means average over the angle ϕ and $t = T/T_c$. We have extended this expression to include the orbital suppression of the magnetic field as follows

$$\log t = \left\langle \int_0^\infty du \, \frac{\cos(\tilde{H}(\phi)u/H_P t)\exp(-Hu^2/H_P t^2 \alpha_m) - 1}{\sinh(u)} \right\rangle_\phi \tag{S12}$$

, where $\alpha_m = \sqrt{2}\, H_{\text{orb}}/H_P$ is the Maki parameter, $H_P = \sqrt{2}\Delta/(g_{ab}\mu_B)$, and $H_{\text{orb}} = 2e^{-\gamma}T_c^2\Phi_0\pi/\tilde{v}_F^2$. This expression was used to fit the upper critical field curve for the state Δ_e for in-plane fields using $\tilde{\alpha}$ and α_m as fitting parameters. The value $H_{\text{orb}} = 7.4$ T found using the WWH formula as discussed in the main text was used. The fitting parameters chosen where $\tilde{\alpha} = 3.4$ and $\alpha_m = 7.1$.

Even-parity state with c-axis field

For this field orientation, the pseudospin magnetic field magnitude is

$$\tilde{H}_z = \frac{H_z}{\sqrt{1+\tilde{\alpha}^2}}. \tag{S13}$$

This immediately yields

$$\frac{H_P^c}{H_P^0} = \sqrt{1+\tilde{\alpha}^2} \tag{S14}$$

, where $H_P{}^0 = \sqrt{2}\Delta/(g_c\mu_B)$ showing the enhancement of the Pauli field for this field orientation. Including the orbital field, yields the expression for the critical field

$$\log t = \int_0^\infty du \frac{\cos(Hu/t)\exp(-Hu^2/t^2\alpha_m)-1}{\sinh(u)}. \tag{S15}$$

This expression was used to determine the upper critical field for Δ_e for the field along the c-axis. Here the value for $\tilde{\alpha} = 3.4$, $g_{ab}/g_c = 1.43/1.11$ (See the section <u>Determination of the g-factor</u>) (yielding $H_P{}^0 = 1.90$), and $H_{orb} = 17.2$ T were used.

<u>Odd-parity state with c-axis field</u>
Now let us turn to the spin-triplet state Δ_o for the field along the c-axis. As explained above (just below Eq. S4), for this field orientation, Δ_o has no Pauli suppression. Consequently, there is only an orbital suppression for this state and we use

$$\log t = \int_0^\infty du \frac{\exp(-Hu^2/t^2\alpha_m)-1}{\sinh(u)}. \tag{S16}$$

To compute the upper critical field in this case requires $T_{c,o}$, the transition temperature for the odd-parity state and also $H_{orb,o}$, the upper critical field for the odd-parity state. Given that the physics for both the even-parity and odd-parity state are the same when there is no c-axis coupling, it is reasonable to find $T_{c,o}$ and $H_{orb,o}$ from the even-parity values by choosing a scale factor of the ratio of $|\Delta_o|/|\Delta_e|$. Here we set $T_{c,o} = 0.87\ T_{c,e}$, and $H_{orb,o} = 17.7$ T.

<u>Determination of the first order boundary from the even to odd-parity state</u>
To find the phase boundary between the even and odd-parity states, the free energy for these states in a magnetic field must be determined. Given that the even-parity state exhibits strong Pauli paramagnetism and that the phase boundary occurs at relatively low fields for the odd-parity state, we ignore the role of vortices in this analysis. In particular, we use the free energy of a superconductor in a Zeeman field

$$f_i = \frac{\Delta^2}{\lambda_i} - 4\pi k_B T \Re \sum_{n=0}^\infty \left[\sqrt{\tilde{\omega}_n^2 + \Delta^2} - \tilde{\omega}_n\right] \tag{S17}$$

9

, where $\widetilde{\omega}_n = \omega_n + i g_c \mu_B \widetilde{H}_z$, $\omega_n = k_B T \pi (2n+1)$, and $\lambda_i = N(0) V_i$ (the index i refers to even or odd parity). For the even-parity state we take $\widetilde{H}_z$ as given by Eq. S13. For the odd-parity state we take $\widetilde{H}_z = 0$ and $T_{c,o} = 0.74\, T_{c,e}$ ($T_{c,o}$ here corresponds to the temperature at which the two critical field lines cross – this implicitly accounts for some reduction in the triplet gap due to orbital effects, leading to a lower ratio than before). The first-order boundary is found by setting $f_e = f_o$.

Determination of the g-factor

The anisotropic g-factors used to estimate the Pauli limiting fields were obtained from the dc-magnetic susceptibility (χ_S) and the specific heat as follow. For the spin-1/2 ($J = 1/2$) single-ion Kondo system, the Wilson ratio written as

$$R_W = \frac{\pi^2 k_B^2}{\mu_0 (\mu_{eff})^2} \frac{\chi_s}{\gamma}$$

, where $(\mu_{\text{eff}})^2 = g^2 \mu_B^2 J(J+1)$ and μ_0 is the magnetic permeability of vacuum, is given to be 2 (Ref. 57). The Wilson ratio for the Kondo-lattice $CeRh_2As_2$ system is expected to be close to this value as the system does not include strong spin-spin interactions. The magnetic susceptibility (χ_s) for $H \parallel c$ is almost saturated below 10 K and reached to $\sim 8.4 \times 10^{-3}$ emu/mol. For $H \parallel ab$, the χ_s tends to saturate upon cooling but diverges in the zero T limit. The saturation value is estimated to be 1.4×10^{-2} emu/mol. The Sommerfeld coefficient (γ) is estimated to be ~ 1 J/mol-K^2 from the specific heat data at high fields in the zero T limit where superconductivity completely vanishes for $H \parallel ab$. From the assumed value of $R_W = 2$, the effective magnetic moments are deduced to be 1.24 μ_B (0.96 μ_B) for $H \parallel ab$ ($H \parallel c$). Accordingly, the saturated moments ($\mu_{\text{sat}} = \mu_{\text{eff}} / \sqrt{3}$) are 0.71 μ_B (0.55 μ_B) and the resultant g-factors are 1.43 and 1.11 for $H \parallel ab$ and $H \parallel c$, respectively.

The μ_{sat} can be alternatively estimated from the wavefunction of the ground state of the localized f-orbital crystal electric field configuration of Ce, as described in the above section. These values are 0.790 μ_B and 0.543 μ_B for $H \parallel ab$ and $H \parallel c$, respectively, consistent with the values from the R_W.

Estimation of the Maki parameter from normal state properties

The Maki parameter obtained from the fit agrees with an estimation in the dirty limit from normal state properties $\alpha_m = 2 e^2 \hbar \gamma \rho_n / 2 m_e \pi^2 k_B^2 V_{\text{mol}} = 5.7$ (Ref. 23), with the electronic charge e, Planck's constant divided by 2π $\hbar$, the specific-heat Sommerfeld coefficient just above the superconducting state $\gamma = 1$ J/mol-K^2, the normal state resistivity of samples of the same batch $\rho_n = 13.3$ $\mu\Omega$cm, the electron mass m_e, the Boltzmann constant k_B, and the molar volume $V_{\text{mol}} = 545 \times 10^{-7}$ m^3/mol. A large Maki parameter usually characterizes systems which are susceptible to going into a state with a modulated SC order parameter, i.e. a Fulde-Ferrell-Larkin-Ovchinnikov (FFLO) state, if they are clean enough (58,59). For our samples with a relatively large ρ_0 this is unlikely and the kink feature is not typical for an FFLO state where a smooth upturn is expected. Note that we don't detect the helical phase expected for in-plane fields (29).

Relation between slopes of transition lines and specific heat jump at a tricritical point.

In the following, we assume that the lines separating the superconducting states 1 and 2 from the normal state N (lines 1-N and 2-N, respectively) are second order and the line separating the two superconducting states (line 1-2) is first order as shown in the schematic phase diagram (Fig. S8). Following the literature (*34*), the slopes of the transition lines near the multicritical point $p_1 = (dH/dT)_{1-N}$, $p_2 = (dH/dT)_{2-N}$, and $p_3 = (dH/dT)_{1-2}$ are related by

$$ p_3 = p_1 \left(\frac{r-1}{r-y} \right) $$

where r is given by the squareroot of the ratio of the specific heat jumps $r = (\Delta C_{1-N}/\Delta C_{2-N})^{1/2}$, and $y = |p_1|/|p_2| < 1$. We extract the slopes from the susceptibility measurements, since the relative error bar between two measurements at constant field or constant temperature is lowest there. We find experimentally $p_1 = (-25 \pm 5)$ T/K, $p_2 < -1000$ T/K and $p_3 = (2 \pm 1)$ T/K. Since $|p_1| \ll |p_2|$ this implies that $y \approx 0$ and $p_3/p_1 \approx -0.08 = (r-1)/r$ so that $r \approx 0.92$. Hence the specific heat jump $\Delta C_{1-N} = (0.85 \pm 0.1) \Delta C_{2-N}$ where $\Delta C_{1-N} = \Delta C(H < H_{kink})$ and $\Delta C_{2-N} = \Delta C(H > H_{kink})$ (See Fig. S4).
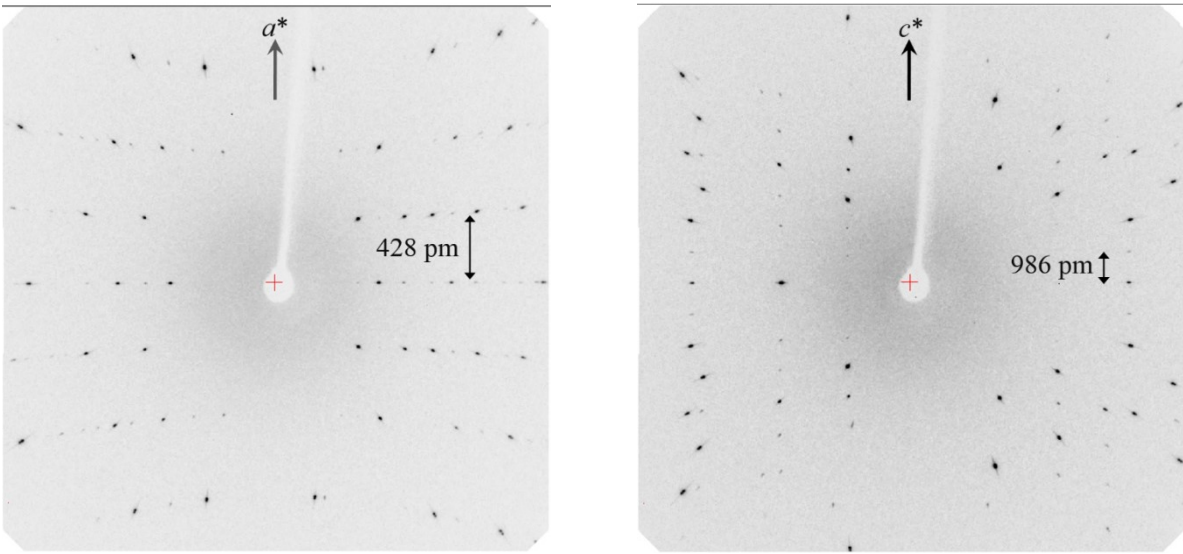
Fig. S1.
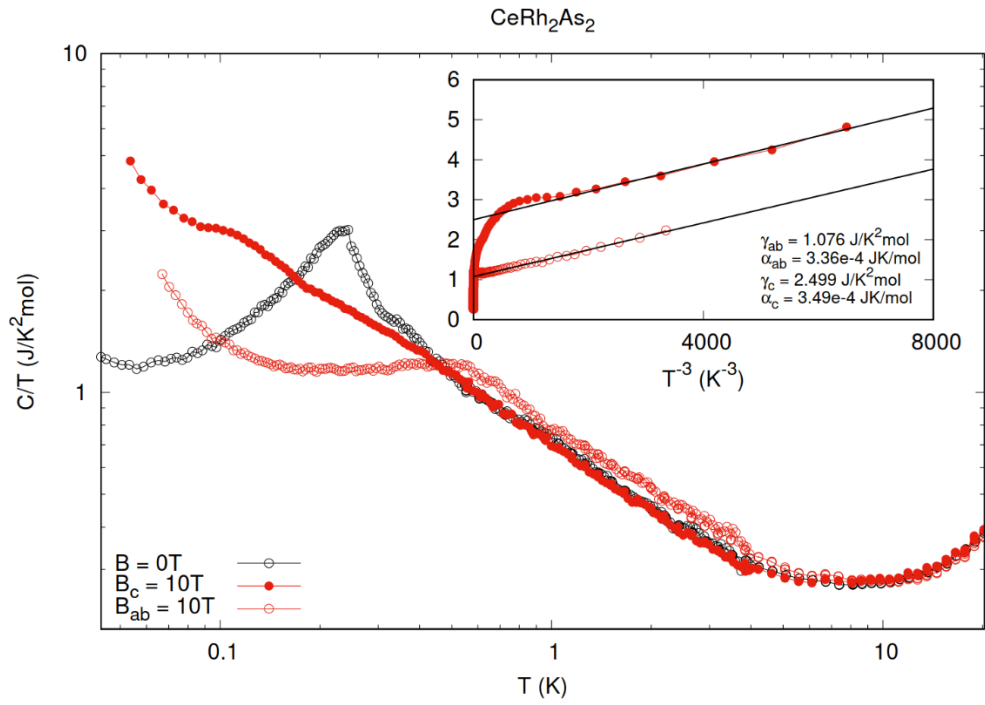CeRh$_2$As$_2$ single crystal axial images (Mo Kα radiation).

Fig. S2.

Specific heat of CeRh$_2$As$_2$ measured in zero magnetic field and in a field of 10 T aligned along both the crystallographic c-axis (filled red circles) and the ab-plane (empty red circles). Inset: Plot of C/T vs T^{-3} with linear fits for the lowest temperature data.
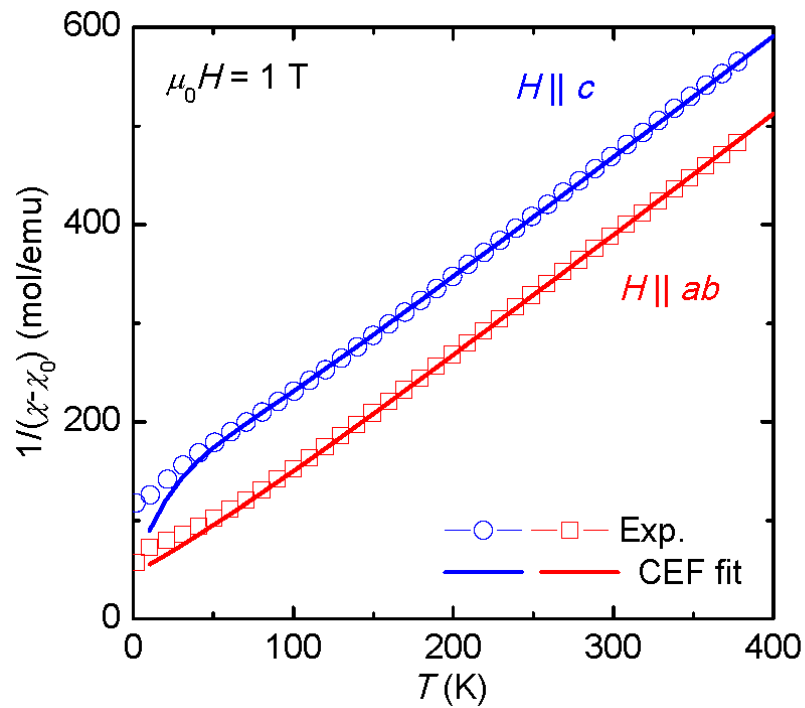
Fig. S3.

Inverse magnetic susceptibility in single crystalline CeRh$_2$As$_2$ and the model fits for the crystal electric field configuration of Ce (see the supplementary text).
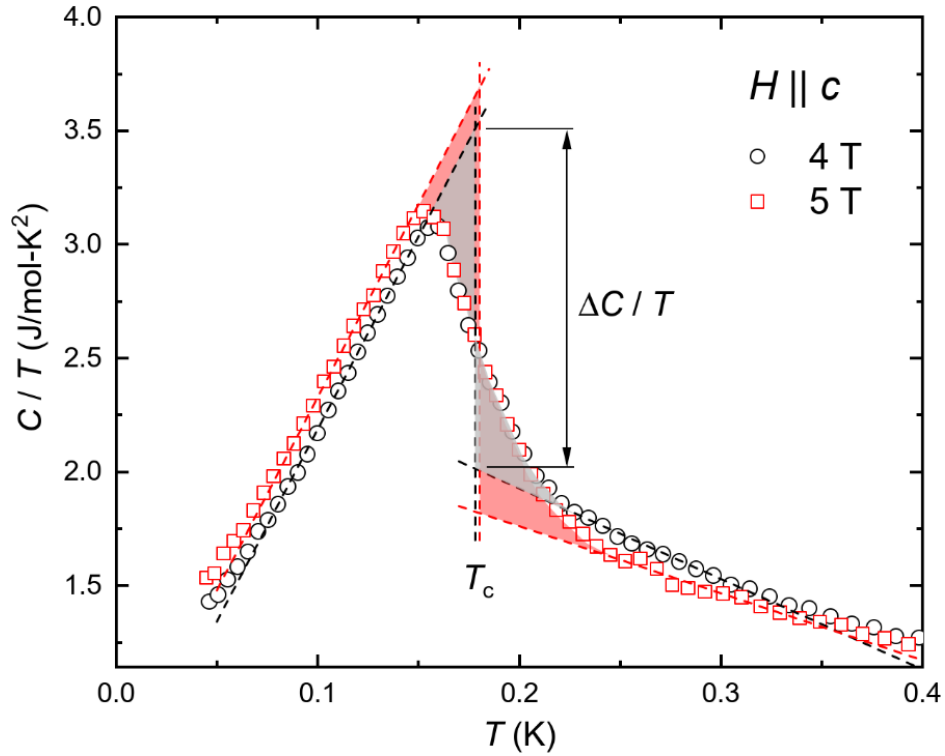
Fig. S4.

C/T data in 4 and 5 T for $H \parallel c$ and the example of the determination of a thermodynamic bulk T_c from the entropy balance. T_c is defined at the midpoint of the C/T jump to lead to the same areas enclosed by the experimental data and the linearly interpolated lines below and above the jump to T_c. The $\Delta C/T$ value is enhanced from 1.49 J/mol-K^2 to 1.87 J/mol-K^2 when the field increases from 4 to 5 T. From these data, the change of the jump can be estimated to $\Delta C(4\text{T})/\Delta C(5\text{T}) \approx$ 0.8, in agreement with the expected change calculated from the slopes of the transition lines in the phase diagram (see the supplementary text).
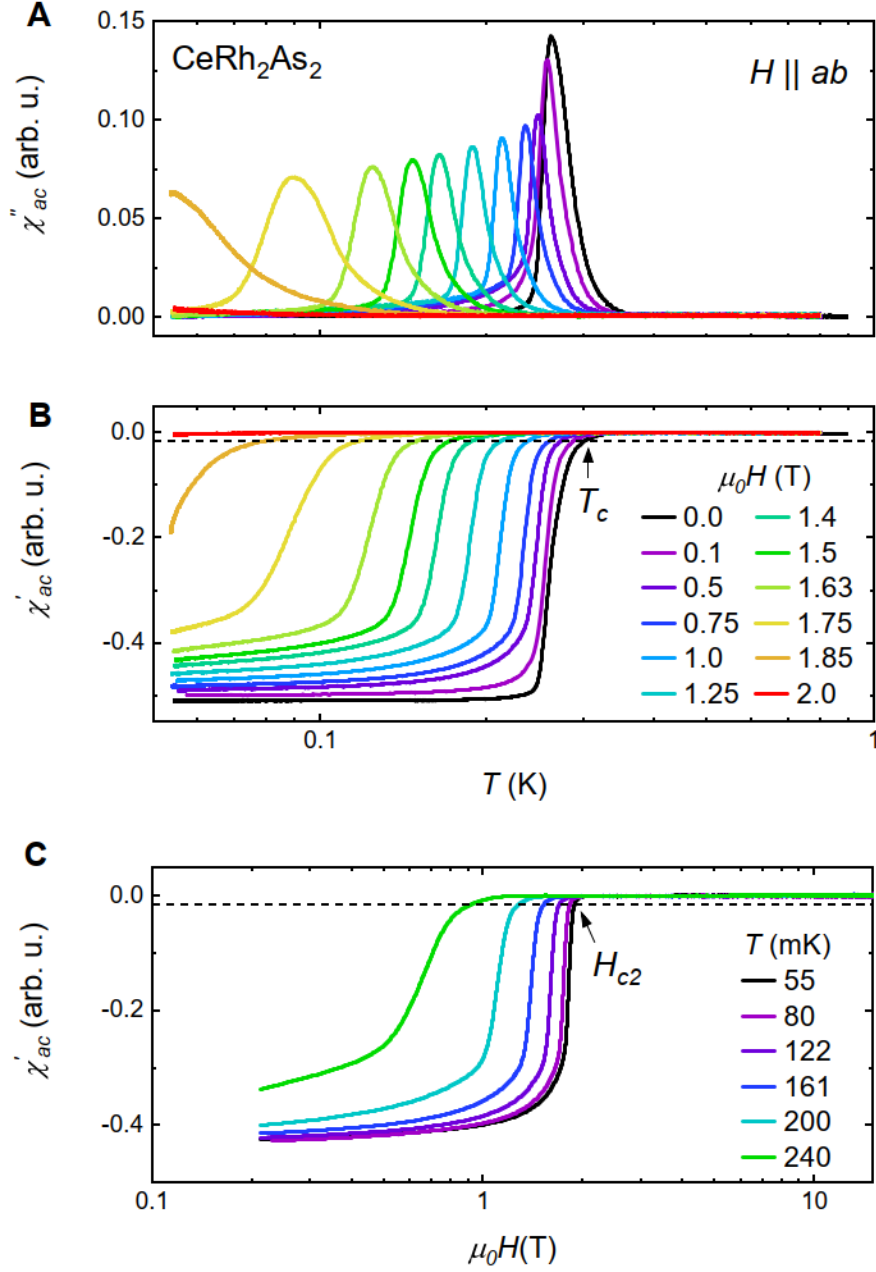
Fig. S5.

Complete data set of magnetic ac-susceptibility in $H \parallel ab$. **A,B,** The temperature dependence of the imaginary and real part signal in various magnetic fields. **C,** Field dependence of the real part signal in various temperatures. The horizontal dotted lines in (B) and (C) denote the criterion to choose T_c and H_{c2}, respectively.
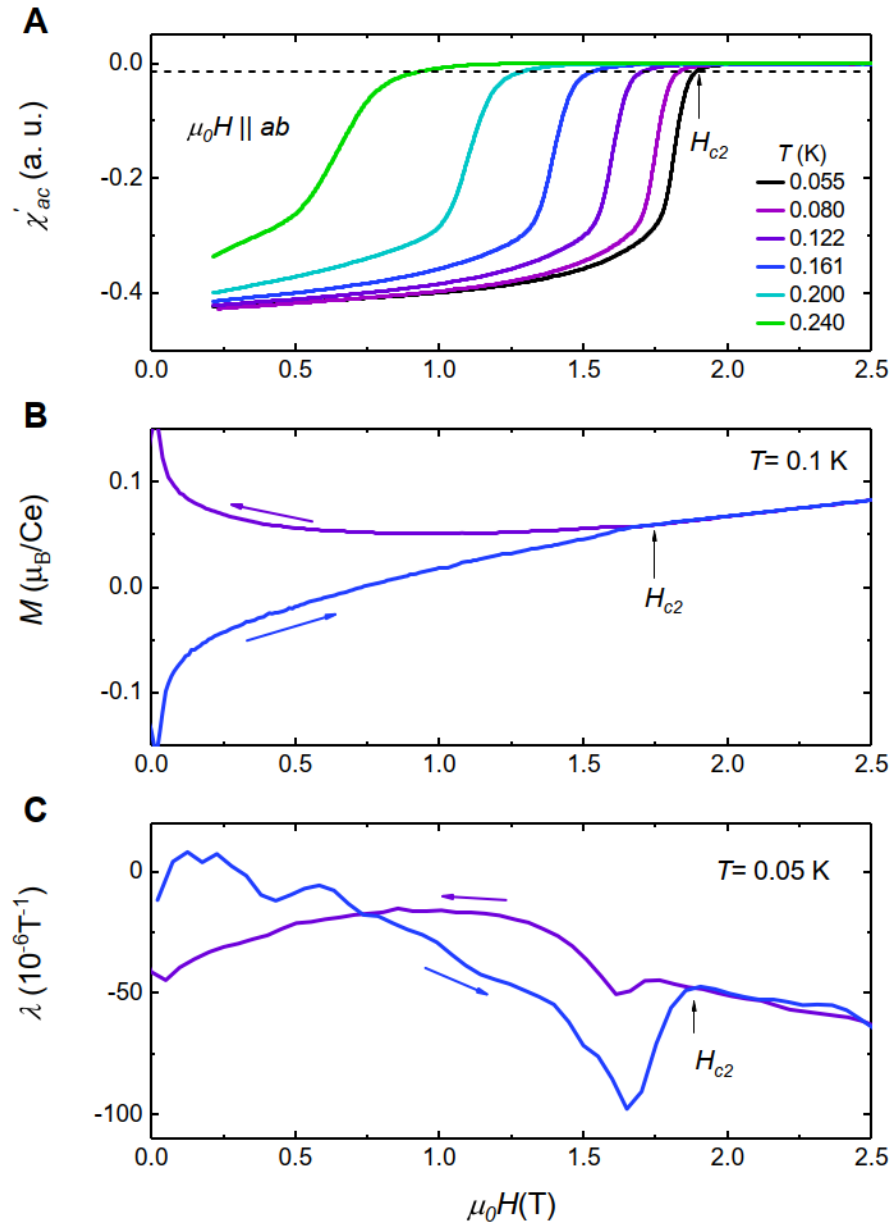
Fig. S6.

Field-dependent measurements in *H ∥ ab*. **A**, magnetic ac-susceptibility for different temperatures. **B**, magnetization at 0.1 K. **C**, magnetostriction at 0.05 K.
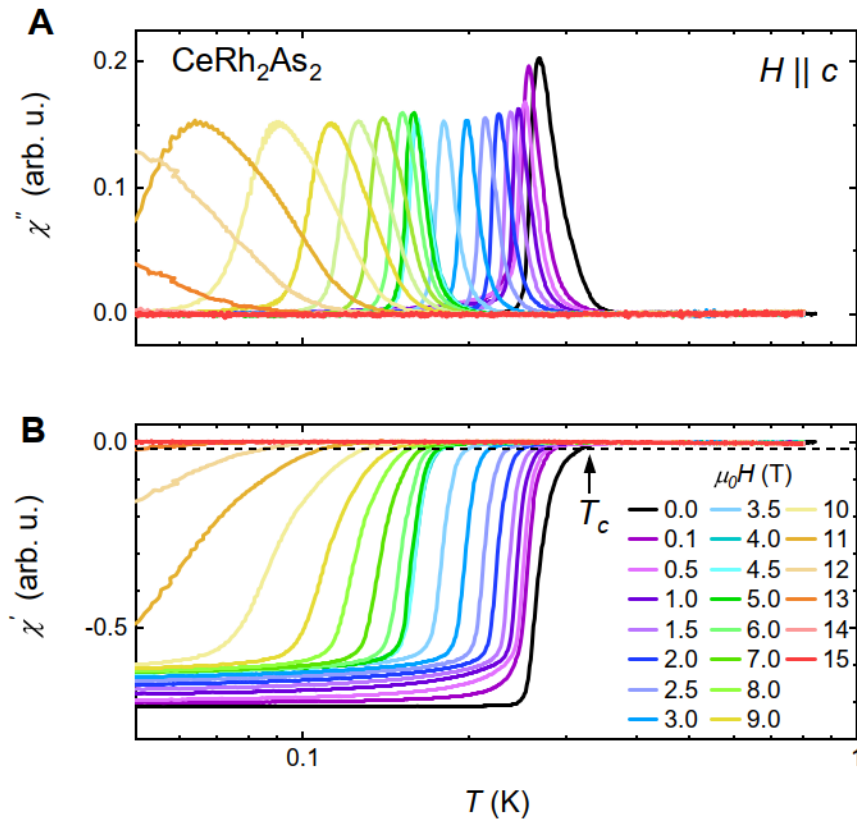
Fig. S7.

Complete data set of magnetic ac-susceptibility in $H \parallel c$. **A,B,** The temperature dependence of the imaginary and real part signal in various magnetic fields. The horizontal dotted line in (B) denote the criterion to choose T_c.
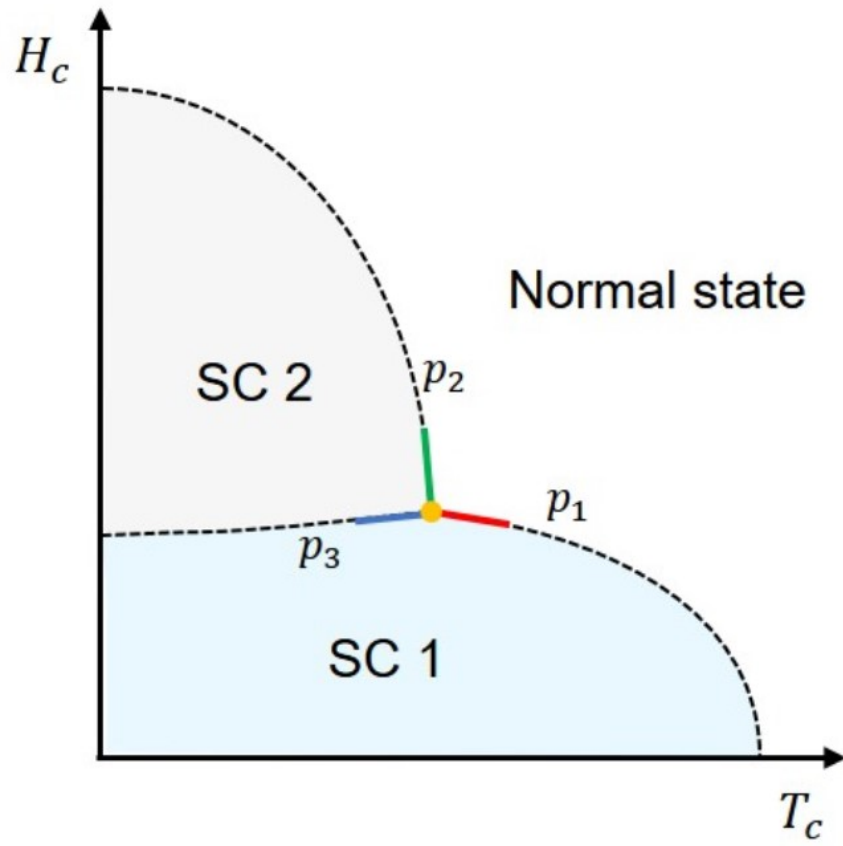
Fig. S8.
Schematic phase diagram for $H \parallel c$. Here we show the relationship of the slopes between SC1, SC2, and the normal state.

Table S1.

Crystallographic data and details of the crystal structure analysis (*45*)

Formula; molar mass	$CeRh_2As_2$; 495.77 amu
Crystal	Metallic prism; $0.076 \times 0.071 \times 0.047$ mm^3
Space group; formula units	$P4/nmm$ (No.129, origin at center); $Z = 2$
Lattice parameter (294 K)*	$a = 428.01(2)$ pm
	$c = 986.16(5)$ pm
Volume; density	$180.66(2) \times 10^6$ pm^3; 9.114 g cm^{-3}
Data collection	Rigaku AFC7 diffraction system, Saturn 724+ detector
	Mo Kα radiation $\lambda = 71.073$ pm, graphite monochromator
	900 exposures, $\Delta\varphi = 0.8°$
Structure refinement	SHELXL-97 (*60*) as implemented in WinGX (*61*)
	Full-matrix least-squares on F^2 (15 parameters)
Absorption correction	Empirical ($\mu = 39.32$ mm^{-1})
Max. and min. transmission	0.1575 and 0.0504
Measured/unique reflections	3617 / 435
R_{int}	0.048
Observed reflections (Fo > 4.0 σ(Fo))	398
$R(F)$; $wR2$	0.028; 0.062
Goof = S =	1.052
$\Delta\rho_{max}$	3.44 e Å^{-3}
$\Delta\rho_{min}$	-5.40 e Å^{-3}

  *Refined on 40 reflections from powder diffraction data using the WinCSD software package (*62*) and LaB$_6$ as internal standard ($a = 415.69(1)$ pm)

Table S2.

Atomic coordinates and anisotropic displacement parameters (ADP) U_{ij} (pm^2) for CeRh$_2$As$_2$ (*45*). U_{eq} is defined as one third of the orthogonalized U_{ij} tensor. The anisotropic displacement factor exponent taken the form: $[-2\pi^2(h^2a^{*2}U_{11} +...+ 2hka^*b^*U_{12})]$. $U_{23} = U_{13} = U_{12} = 0$.

Atom	Site	x	y	z	U_{eq}	U_{11}	U_{22}	U_{33}
Ce(1)	2*c*	¼	¼	0.75469(3)	66(1)	71(1)	U_{11}	56(2)
Rh(1)	2*a*	¾	¼	½	76(1)	86(1)	U_{11}	54(2)
Rh(2)	2*c*	¼	¼	0.11741(4)	71(1)	77(1)	U_{11}	60(2)
As(1)	2*a*	¾	¼	0	70(1)	69(2)	U_{11}	72(3)
As(2)	2*c*	¼	¼	0.36405(6)	65(1)	72(2)	U_{11}	51(2)